Applied Thermal Engineering 246 (2024) 122879

Contents lists available at ScienceDirect

Applied Thermal Engineering

journal homepage: www.elsevier.com/locate/apthermeng

Research Paper

Numerical heat generation analysis of the tabbed and novel tabless designs of cylindrical-type lithium-ion batteries

Chika Eze [a,b], Jingyuan Zhao [c], Dukhyun Chung [d,*], Mohammad Fakhimi Bonab [b], Abel Chuang [b,*], Andrew F. Burke [c,*], Guanhua Chen [a,e,*]

[a] Hong Kong Quantum AI Lab, 17 Science Park West Avenue, Hong Kong, China
[b] Department of Mechanical Engineering, University of California, Merced, CA, USA
[c] Institute of Transportation Studies, University of California, Davis, CA, USA
[d] Department of Mechanical Engineering, Chungnam National University, Daejeon, South Korea
[e] Department of Chemistry, The University of Hong Kong, Hong Kong, China

ARTICLE INFO

Keywords:
Li-ion battery
Cylindrical cell
Heat generation
Tabbed design
Tabless design

ABSTRACT

The heat generation behaviours of a traditional tabbed cylindrical lithium-ion (Li-ion) battery are known to greatly affect its performance, cycle life, and safety. In this study, we explore the heat generation behaviours of the tabbed and novel tabless designs of a 21,700 cylindrical cell with graphite anode and NCA/LiNi0.8-Co0.15Al0.05O2 cathode, by coupling the discreet layers of a three-dimensional (3D) disassembled electrochemical (EC) model with a two-dimensional (2D) axisymmetric heat transfer (HT) model. The respective heat generation mechanisms of each battery components of tabbed and tabless designs are first compared, and it is observed that the tabbed design generates significantly more heat than the tabless design, with the negative current collectors (NCC) in the tabbed design accounting for over 80 % of the total heats at 1C-rate. Also, the tabless design reduces the cell voltage drop due to its lower ohmic impedance and promotes a more homogenous cell temperature than the tabbed design. Next, the effects of particle size (ω) for the tabless design on the ohmic, reversible, and polarization heats of the battery's electrodes are investigated at a high discharge rate of 10C, and the results show that polarisation heat decreases significantly in both electrodes as ω decreases. At the Negative Electrode (NE), the ohmic heating decreases initially as ω decreases because the battery is not drawing significant current. As the current drawn increases, Li-ion transport resistance also increases and at depth of discharge (DoD) = 36 %, a reverse in the trend is observed leading to an increase in Ohmic heating up to the end of life. In contrast, the ohmic heating at the Positive Electrode (PE) increases throughout the discharge process as ω decreases. For the reversible heat, the heat is negative in the NE side initially and fluctuates with ω towards the end of life (DOD = 88 %) when it changes from heat sink to heat source, whereas in the PE it remains unchanged for all ω throughout the discharge process. The resulting temperature drop is caused by the increase in the overall reversible heat sink effect in the NE side, as well as the weakened polarization heat in both electrodes. On the other hand, miniaturising the electrode thickness (η) causes a considerable decrease in ohmic heating in both electrodes resulting in larger temperature drops and elevated voltage curve. This study provides relevant insights in support of the development of battery thermal management systems (BTMS) for the tabbed and novel tabless batteries in a realistic environment.

1. Introduction

Electrified transportations including the electric vehicles (EVs) have recently emerged as one of the leading options for addressing the concerns of the global energy crisis and climate change [1,2]. Currently, few areas in the world of clean energies are as active as the EV market. According to the international energy agency (IEA), sales of EVs doubled from 2020 to 2021, reaching a new record of 6.6 million, bringing the total number of electric cars on the road to 16.5 million. Sales of EVs increased by 13 % in the first half of 2022, with 2 million EVs sold in the first quarter alone, a 75 percent increase and based on Net Zero Emission strategy, an electric car fleet of over 300 million is also projected by the

* Corresponding authors.
E-mail addresses: dhchung@cnu.ac.kr (D. Chung), abel.chuang@ucmerced.edu (A. Chuang), afburke@ucdavis.edu (A.F. Burke), ghc@everest.hku.hk (G. Chen).

https://doi.org/10.1016/j.applthermaleng.2024.122879
Received 29 April 2023; Received in revised form 20 November 2023; Accepted 4 March 2024
Available online 6 March 2024

year 2030 [3]. Due to their high-power density, long lifespan, and high efficiency, lithium-ion (Li-ion) batteries are the most commonly used power source for EVs [4]. However, for Li-ion batteries, temperature is a key factor in the performance, safety, and cycle life of cells [5–7]. The optimal working temperature for Li-ion batteries is within the range 25 ~ 40 °C [8–10]. However, during charge/discharge process, the undesirable heat generation that takes place inside Li-ion batteries could elevate the temperature of the battery beyond the optimal range, and this might lead to disastrous consequences such as the thermal runaway problems [11–13]. Specifically, high temperatures intensify side reactions, hasten battery degradation, and even result in explosion of EVs [5]. On the other hand, when the temperature is low (<15 °C), the discharge capacity is largely reduced due to the increased internal resistance and reduced electrochemical (EC) reaction kinetics. Also, at low temperature, lithium plating might occur due to a reduction in ionic conductivity of the solid electrolyte interphase (SEI), and a possible short circuit caused by the growth of lithium dendrite in the anode side especially at sub-zero temperatures. Apart from the issues of high and low temperatures in Li-ion batteries, temperature non-homogeneity is also a cause for concern as the non-uniform temperature distribution will lower the cycle life of a Li-ion battery and cause capacity decay [14]. Also, for EVs to compete more effectively in the transportation markets and alleviate range anxiety, faster charging rates must be adopted. Again, this increases the heat generation rate and ultimately puts substantial thermal limits on the battery packs [15–20]. Since thermal behaviour is crucial to battery cycle life and safety during fast charging, research toward the development of fast charging protocols that reduce heat generation and temperature rise should also be considered [21]. Hence, developing new, fast charging protocols that can reduce heat generation and preserve battery life is of high interest for the EV market. To this end, it is essential to gain a profound understanding of the heat generation characteristics of Li-ion batteries based on the interactive EC and heat transfer (HT) coupled behaviours, especially at high C-rate, during which enormous heats are generated [22–24].

Inherently, two main factors influence the overall thermal behaviour of a cell – a) the thermal boundary conditions, which is determined by the design of battery thermal management systems (BTMS) [25] and b) the internal heat generation, influenced by the cell design [26]. The design of a good BTMS for a battery pack considers the influence of the cooling media, and the overall BTMS architectures on both the maximum temperature of the pack and the inter/intra-cell temperature homogeneity [27–30]. Therefore, complexity and costs of BTMS designs is a major issue to contend with [31,32]. In addition to the thermal boundary conditions, the internal cell design, such as the number and position and configuration of the current collecting tabs, also play an important role in the cell thermal behaviour [26,33].

Several automakers have announced plans to use large-format cylindrical Li-ion cells with innovative tab designs in future vehicle generations. Adopting larger cell formats can improve driving range and lower manufacturing costs because larger cells have higher volumetric energy density at the cell and module levels, but this also introduces new thermal challenges [34,35]. Nonetheless, optimizing macroscopic design aspects such as electrode material geometry and tab design could potentially address larger format thermal issues while increasing charging speeds [36], safety [37], and cycle life [38]. For cylindrical cells, previous computational [39,40] and experimental studies [33] have demonstrated that increasing the number of tabs reduces temperature rise and thermal gradients compared to a single pair of tabs. This is because electrons generated on the current collectors travel a shorter distance before being collected by tabs, resulting in a significantly weakened ohmic resistance. In 2019, one of the leaders in global sales of EVs, Tesla Inc. filed a patent on the fabrication of cylindrical cells employing a novel 'tabless' design by removing the additional metal strip tabs and instead letting the metal current collector foils conduct the current to the outside. This revolutionary design is anticipated to substantially enhance the performance of the cell by delivering a greater range on the pack level (+14 %), reducing the cost per kWh (−14 %) due to the form factor and tab design, and increasing production speed [41]. More importantly, this design promises to massively reduce the polarization drops and heat generation inside the current collectors, thereby eliminating the ohmic heating-the dominant type of internal heat generation in a large battery cell [41].

Generally, EC - HT coupled battery models are a cost-effective yet powerful modelling tool to investigate the EC and HT characteristics of Li-ion batteries. Hence, to understand and predict the EC-HT behaviour of Li-ion batteries, a variety of finite element (FEM) based models of various dimensions are usually coupled. While most of the existing FEM EC models are built using the pseudo-two-dimensional (P2D) model, which is based on the kinetics equations, concentrated solution theory, and porous electrode theory [42–45]. Fourier's law and the energy conservation equation form the basis for HT model, and 2D-Axisymmetric or 3D geometry is typically considered as the research object for this model. Due to the realistic consideration of the coupled interaction between the EC and HT properties, such models can explain the effects of phenomena such as overpotential, local current density, and other EC characteristics on the heat generation rate of Li-ion batteries [46]. In this approach, however, the battery component's non-homogeneities and current collector effects within the electrode plane are ignored. Although this simplification might be useful for small-scale batteries, it is quite unreasonable for large scale batteries modelling, and almost impossible to model tabless designs.

In this study, we innovatively develop a comprehensive model to understand the contribution from each material components of the 21,700 cylindrical NCA battery to the internal heat generation by coupling for the first time, discreet layers of a three-dimensional disassembled EC model with a two-dimensional axisymmetric HT model. Based on this model, we explore the heat generation behaviours of the 21,700 tabless designs under very high C-rate (10C) discharge protocols. Additionally, the influence of electrode thickness and particle radius on heat generation mechanisms for the tabless designs are also examined under the high C-rate conditions. Overall, this work provides a qualitative understanding of heat transfer to tabbed and tabless designs of 21,700Li-ion batteries, and the results presented here will serve as a reference guide in the design of the novel tabless 4680 cells, which the modelling and experimental data are lacking in literature. The obtained results may find use in the quest for internal cooling of the battery cell, eliminating the need for an expensive and complex BTMS.

2. Methodology

Due to its higher energy content and lower production cost, the 21,700-format is becoming the new standard for cylindrical Li-ion batteries [47], in comparison to the conventional 18,650-type batteries. According to J. B. Quinn et al. [48], thermal management of 21,700-type cells is more challenging than that of 18,650-type cells due to a greater volume-to-surface ratio and a greater active-to-non-active material ratio. By this metric, this means that the thermal management for the revolutionary 4680 cells will be even more difficult than that of 21,700 cells. Therefore, a model implemented for 21,700 and 4680-type batteries are therefore more interesting for thermal development studies. Furthermore, such a model will be especially useful for studies on fast charging scenarios and for providing the necessary information for the development of a relevant BTMS in a realistic environment.

2.1. Models descriptions

To investigate the interactive EC and HT characteristics of cylindrical-type Li-ion batteries under natural convection conditions, a 3D EC - HT coupled model is developed for 21,700 cells in COMSOL Multiphysics® version 5.5, using a direct time-dependent solver of PARDISO to obtain the numerical solution. Fig. 1 (a) depicts the

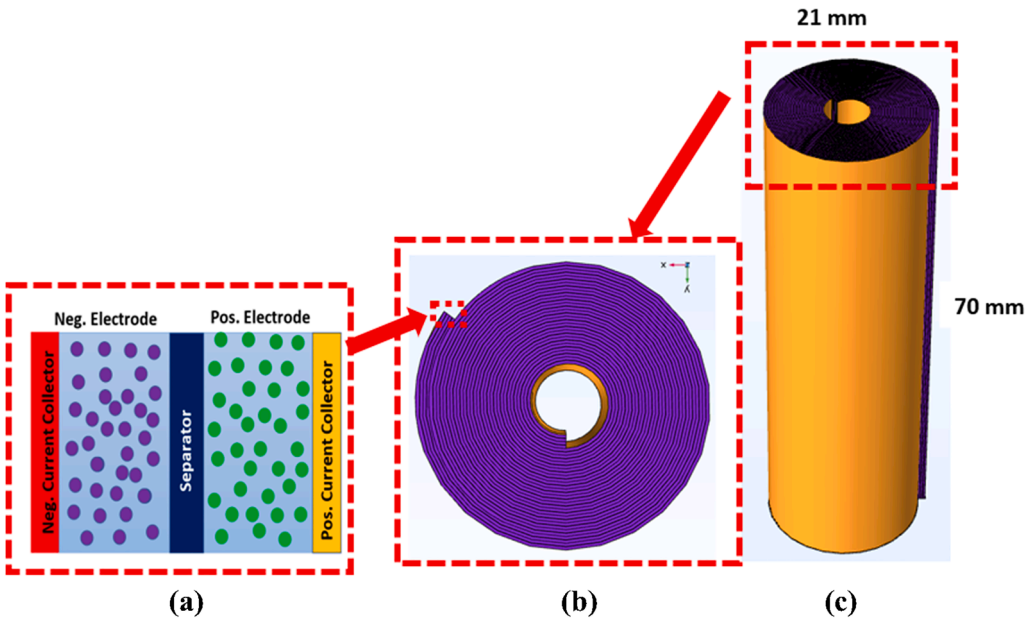

Fig. 1. Schematic diagram of (a) partially enlarged drawing showing five domains of the Li-ion EC model (b) 2D cross-section showing the spirally wound internal structure (c) computational domain for the 3D model of the 21,700 cells.

structure of a typical cylindrical Li-ion battery, which consists of various functional layers wound up in the shape of a jelly roll: positive current collector (PCC), positive electrode (PE), separator (SEP), negative electrode (NE), and negative current collector (NCC). The cells with a nominal capacity of 4.5 Ah which is composed of graphite as NE and NCA (LiNi0.8Co0.15Al0.05O2) as PE. The electrolyte consists of 1 M LiPF6 in an EC/EMC (3:7) solvent mixture. The voltage between 2.5 V and 4.2 V is allowed by the manufacturer, with a nominal voltage of 3.6 V. The battery is 21 mm in diameter and 70 mm in height, as shown in Fig. 1. Since two adjacent cell units share a current collector, each cell unit only contains half of the current collector. The design of 3D EC layered sub-model is coupled with a 2D axi-symmetric layered HT model of the entire battery, which consists of several stacked cell units. For the tabbed design, only a pair of positive and negative tabs were modelled at both ends of the current collectors. Whereas for the tabless design, several numbers of integrated tabs were uniformly installed across the entire positive and NCC to mimic the so-called tabless design (which is just a continuous tabbing concept). For both designs, the heat generation of the entire battery including the tabbed and tabless battery designs were described using the EC reaction and the physical property parameters of the battery (Table 1).

2.2. Governing equations

The mathematical description of the EC - HT coupled model is based on the conservations of mass, charge, and energy.

The following assumptions are made to simplify the governing equations of the model [47].

(1) Active material particles in both positive and NE are considered as identical spheres of uniform size.

(2) The volume change of the electrode during the discharge process is ignored.

(3) No gas is generated during the discharge process.

(4) All side reactions are negligible.

(5) The formation of the solid electrolyte interphase (SEI) layer and lithium dendrites is neglected.

(6) The contact thermal resistance among different materials is ignored.

(7) The thermal radiation of the battery is not considered.

2.3. Mass conservation

2.3.1. Solid phase

A typical Li-ion battery unit, according to the porous electrode theory [44,49], consists of the solid phase in the electrode material and the liquid phase in the electrolyte, with the electrode material and electrolyte regarded as superimposed continua. [50]. Fick's law is applied to describe the mass balance of Li-ion in the electrode active particles, which can be expressed as:

$$\frac{\partial c_s}{\partial t} = \frac{D_s}{r^2}\frac{\partial}{\partial r}\left(r^2\frac{\partial c_s}{\partial r}\right) \tag{1}$$

where r is the particle radius, t is the time, C_s is the concentration of the intercalated lithium in the solid phase, D_s is the diffusion coefficient of lithium in the solid phase.

The diffusion flux of the Li-ion in the centres of the spherical particles and that on the surfaces of particles can be described as follows:

$$-D_s\frac{\partial c_s}{\partial r}\bigg|_{r=0} = 0 \tag{2}$$

$$-D_s\frac{\partial c_s}{\partial r}\bigg|_{r=rp} = \frac{S_a \times i_{loc}}{F} \tag{3}$$

where $S_a = 3 \times \epsilon_s / R_s$ is the specific area of the porous electrode and $\boldsymbol{i_{loc}}$ is the current density generated by Li intercalation/deintercalation at the surface of active particles.

2.3.2. Liquid phase

The concentrated solution theory is used to model the mass balance of Li-ion in electrolyte as shown below:

$$\varepsilon_l\frac{\partial c_l}{\partial t} + \nabla \bullet \left(-D_l^{eff}\nabla c_l\right) = (1 - t_+) \bullet \frac{S_a \times i_{loc}}{F} \tag{4}$$

where ε_l is the volume fraction of electrolyte in the electrodes and the SEP, $c_{l,k}$ is the concentration of Li-ion in the electrolyte phase, D_l^{eff} is the effective diffusion coefficient of Li-ion in the electrolyte phase. Since there is neither a Li-ion source nor a sink at the interface between current collectors and active material, the boundary conditions can be expressed as follows:

Table 1
The geometrical, EC and HT parameters used in the 3D models.

Parameters	NE	PE	SEP	NCC (Cu foil)	PCC (Al foil)
Design specification					
Thickness, L (μm) [a]	75	60	10	10	20
Particle radius, R (μm) [a]	2.5	0.25	–		
Electrolyte phase volume fraction, $\varepsilon_{l,\ k}$ [b]	0.4	0.25	0.37		
Solid phase volume fraction, $\varepsilon_{s,k}$ [b]	0.428	0. 598			
Bruggeman coefficient [a]	1.5	2	3		
Local state-of-charge in PE at 0 % cell state-of-charge (soc_pos) [a]	0.2				
Local state-of-charge in NE at 100 % cell state-of-charge (soc_neg) [a]	0.8				
Maximum cell voltage, [V] [a]	4.2				
Minimum cell voltage, [V] [a]	2.5				
Ambient Temperature [°C] [a]	20				
Battery height, H_{cell} (mm) [a]	70				
Battery radius, R_{cell} (mm) [a]	10.5				
Mandrel radius, $R_{mandrel}$ (mm) [a]	0.5				
Thickness of out can, d_{can} (mm) [a]	0.2				
Tab height, H_{tab} (mm) [a]	10				
Tab width, W_{tab} (mm) [a]	10				
Cell thickness, L_cell (mm) [c]	L_sep + L_pos + L_neg + L_neg_cc/2 + L_pos_cc/2				
Length of disassembled battery assembly, W_{cell} (mm) [c]	((r_batt-d_can-r_mandrel)Ã·(L_cell)) × (r_batt-d_can + r_mandrel)) × 3.142				
No of turns, N_turns [c]	((r_batt-d_can-r_mandrel)Ã·(2× L_cell))				
Li concentration					
Electrolyte concentration, c_l (mol·m^{-3}) [a]	1200	1200	1200		
Initial solid concentration, $c_{s,initial}$ (mol·m^{-3}) [a]	28,482	11,328	–		
Maximum solid concentration, $c_{s,max}$ (mol·m^{-3}) [a]	35,603	56,640	–		
HT Parameters					
Density, ρ (kg·m^{-3}) [d]	2300	4740	1129.95	8960	2700
Specific heat capacity, c_p (J·kg^{-1} °C^{-1}) [d]	750	1270	2055	385	900
Thermal conductivity (W·m^{-1} °C^{-1}) [d]	1.0	1.04	0.6	400	238

[a] Ref. [54].
[b] Estimated.
[c] Ref. [55].
[d] COMSOL material database.

$$-D_{eff,n}\frac{\partial c_{l,n}}{\partial z}\bigg|_{z=0} = -D_{eff,p}\frac{\partial c_{l,p}}{\partial z}\bigg|_{z=L_{ncc/2}+L_n+L_s+L_p+L_{pcc/2}} = 0 \tag{5}$$

At the left and right neighbourhoods of the contact surface of the electrode and the SEP, the Li-ion fluxes are equal and the corresponding boundary conditions therein can be written as:

$$-D_{eff,n}\frac{\partial c_{l,n}}{\partial z}\bigg|_{z=L_n^-} = -D_{eff,s}\frac{\partial c_{l,s}}{\partial z}\bigg|_{z=L_n^+} \tag{6}$$

$$-D_{eff,s}\frac{\partial s}{\partial z}\bigg|_{z=(L_n+L_s)^-} = -D_{eff,p}\frac{\partial c_{l,p}}{\partial z}\bigg|_{z=(L_n+L_s)^+} \tag{7}$$

At the left and right neighbourhoods of the contact surface of electrode and SEP, the Li-ion concentrations, and the corresponding boundary conditions therein can be written as:

$$c_{l,n}\big|_{z=L_n^-} = c_{l,s}\big|_{z=L_n^+} \tag{8}$$

$$c_{l,s}\big|_{z=(L_n+L_s)^-} = c_{l,p}\big|_{z=(L_n+L_s)^+} \tag{9}$$

2.4. Charge conservation

2.4.1. Solid phase

Charge conservation in the solid electrode materials follows Ohm's law, which can be described by:

$$\nabla \bullet \left(-\sigma_s^{eff}\nabla\Phi_s\right) = -S_a i_{loc} \tag{10}$$

$$\sigma_s^{eff} = \sigma_s \varepsilon_s^{\gamma_s} \tag{11}$$

where σ_s^{eff} represents the effective electric conduction of the electrode, Φ_s is the potential, ε_s is the volume fraction and γ_s is the Bruggeman's tortuosity. At the interface between the PCC and the PE, the charge flux equals the applied current density. In addition, there is no charge transport across the contact surface between the SEP and electrodes. And the NE's reference potential is arbitrarily set to zero. Therefore, the corresponding boundary conditions can be expressed as:

$$-\sigma_p^{eff}\frac{\partial\Phi_p}{\partial z}\bigg|_{z=L_{ncc/2}+L_n+L_s+L_p+L_{pcc/2}} = -I_p \tag{12}$$

$$-\sigma_n^{eff}\frac{\partial\Phi_n}{\partial z}\bigg|_{z=L_n} = -\sigma_p^{eff}\frac{\partial\Phi_p}{\partial z}\bigg|_{z=L_n+L_s} = 0 \tag{13}$$

$$\Phi_s|_{z=0} = 0 \tag{14}$$

2.4.2. Liquid phase

Charge conservation in the electrolyte phase can be derived from the mass transport of charged species in the electrolyte [51]:

$$\nabla \bullet \left(-\sigma_l^{eff}\nabla\Phi_l + \frac{2RT\sigma_l^{eff}}{F}\left(1+\frac{\partial lnf}{\partial lnc_e}\right)(1-t_+)\nabla(lnc_e)\right) = S_a i_{loc} \tag{15}$$

$$\sigma_l^{eff} = \sigma_l \varepsilon_l^{\gamma_l} \tag{16}$$

where f is the electrolyte activity coefficient and t_+ is the transference number for the Li-ions. Since only electrons can pass through the interface between the electrodes and the current collectors, the boundary conditions can be written as:

$$-\frac{\partial\Phi_l}{\partial z}\bigg|_{z=0} = -\frac{\partial\Phi_l}{\partial z}\bigg|_{z=L_{ncc/2}+L_n+L_s+L_p+L_{pcc/2}} = 0 \tag{17}$$

Butler-Volmer electrode kinetics is the term that couples charge balance and material balance. It describes the fundamental relationship between electrical current on an electrode, electrode potential, and local specie concentration at the electrode–electrolyte interface. The Butler-Volmer relationship is denoted as [52]:

$$i_{loc} = i_0\left(\exp\left(\frac{\alpha_a\eta F}{RT}\right) - \left(\exp\left(\frac{-\alpha_c\eta F}{RT}\right)\right)\right) \tag{18}$$

where the exchange current density i_0 is given by:

$$i_0 = FKc_e^{\alpha_a}\left(c_{s,max} - c_{s,surf}\right)^{\alpha_a} c_{s,surf}^{\alpha_c} \tag{19}$$

While the overpotential is given by:

$$\eta = \left(\Phi_s - \Phi_l - E_{eq}\right) \tag{20}$$

And the temperature-dependent open circuit potential of the electrode is approximated by first order Taylor's series expansion given below:

$$E_{eq} = E_{eq,ref}(SOC) + \frac{dE_{eq,ref}}{dT}\left(T - T_{ref}\right) \tag{21}$$

2.5. Two-dimensional-axisymmetric thermal model

During operation, the battery has three main heat sources: reversible

heat (Q_{rev}), and irreversible heat (Q_{irrev}), and ohmic heat (Q_{ohm}) [53]. A battery's total heat generation is therefore defined as:

$$Q_{tot} = Q_{rev} + Q_{irrev} \tag{22}$$

$$Q_{irrev} = Q_{ohm} + Q_{pol} \tag{23}$$

where the ohmic heat Q_{ohm}, is the amount of energy lost due to transport resistance in both the solid and electrolyte phases, and it can be calculated as:

$$Q_{ohm} = \sigma_s^{eff}\nabla\Phi_s{}^2 + \sigma_l^{eff}(\nabla\Phi_l{}^2 + \frac{2RT\sigma_l^{eff}}{F}(1+\frac{\partial lnf}{\partial lnc_e})(1-t_+)\nabla c_e\nabla\Phi_l \tag{24}$$

The polarization heat Q_{pol}, is defined as the energy required to overcome the barrier during the Li intercalation and de-intercalation processes, and it is defined as:

$$Q_{pol} = S_a i_{loc}\eta \tag{25}$$

The reversible heat Q_{rev}, is caused by entropy change in EC reactions and is expressed as:

$$Q_{rev} = S_a i_{loc} T\frac{dE_{eq,ref}}{dT} \tag{26}$$

And the energy conservation equation of this battery can be expressed as:

$$\rho_k C_{p_k}\frac{\partial T_{ave}}{\partial t} = \nabla\bullet\nabla(\lambda_k T_{ave}) + Qtot_k \tag{27}$$

where ρ_k, C_{p_k} and λ_k are the density, the heat capacity, and the thermal conductivity, respectively for each battery material (k = n, p, s, ncc and pcc).

The natural convection boundary condition can be expressed as:

$$-\lambda\nabla T = hA(T - T_{amb}) \tag{28}$$

where A is surface area, and λ is the convective heat transfer coefficient and is set to be 5 $W{\cdot}m^{-2}\,{}^{\circ}C^{-1}$.

2.6. Model parameters

To characterize the impacts of the temperature field on EC behaviour, the following temperature and Li-ion concentration dependent parameters are defined in this work.

The reaction rate constant, as the key factor in the EC reaction, follows the Arrhenius formula [54]:

$$k_s = k_{s,ref}\bullet exp[\frac{(E_{a,R}),s}{R}(\frac{1}{T_{ref}} - \frac{1}{T})] \tag{29}$$

where k_0 is the reaction rate constant of the electrodes under the reference temperature $T_{ref} = 20^{\circ}C$, and $(E_{a,R}),s$ is the reaction activation energy.

The diffusion coefficient of the Li-ion in the electrodes can be expressed as [22]:

$$D_s = D_{s,ref}\bullet exp[\frac{(E_{a,D}),s}{R}(\frac{1}{T_{ref}} - \frac{1}{T})] \tag{30}$$

where $(E_{a,D}),s$ is activation energy for diffusion, and $D_{0,ref}$ is the diffusion coefficient of Li-ion in the electrodes at the reference temperature T_{ref}.

The electrolyte ionic conductivity, diffusion coefficient and activity coefficient are each, a function of both the temperature and the Li-ion concentration in the electrolyte [54], and are defined respectively as:

$$\sigma_l = \sigma_{l,ref}\times int(\frac{c_l}{1[mol/m^3]})\bullet exp[\frac{(E_{a,\sigma}),l}{R}(\frac{1}{T_{ref}} - \frac{1}{T})] \tag{31}$$

$$D_l = D_{l,ref}\times int(\frac{c_l}{1[mol/m^3]})\bullet exp[\frac{(E_{a,D}),l}{R}(\frac{1}{T_{ref}} - \frac{1}{T})] \tag{32}$$

$$f_{\pm} = f_{\pm,ref}\times int(\frac{c_l}{1[mol/m^3]})\bullet exp[\frac{(E_{a,R}),f\pm}{R}(\frac{1}{T_{ref}} - \frac{1}{T})] \tag{33}$$

2.7. Electro-chemical-thermal coupling

In general, to achieve EC - HT coupling, the EC and HT models must be adequately linked in terms of heat generation and temperature. Fig. 2. depicts the 3D EC and 2D axisymmetric HT model's coupling process. Unlike several of the existing models where the volume average of the heat generated in the entire EC model is used as the input of the HT model and the average temperature of lumped winding used to replace the temperature at respective component inside the battery [42–45]. In the present study, the 3D EC model is used to calculate the heat generated from each discreet layer of EC model and directly coupled to the corresponding layer of a 2D axi-symmetric HT model which consists of 29 stacked full cell units, such that at any time t, the following relationships occur:

i. Total Heat generated from NE (Q_{tot}NE) in EC model is coupled to 29 double layers of NE in HT model.
ii. Total Heat generated from PE (Q_{tot}PE) in EC model is coupled to 29 double layers of PE in HT model.
iii. Total Heat generated from SEP (Q_{tot}SEP) in EC model is coupled to 29 double layers of SEP in HT model.
iv. Total Heat generated from PCC (Q_{tot}PCC) in EC model is coupled to 29 single layers of PCC in HT model.
v. Total Heat generated from NE (Q_{tot}NCC) in EC model is coupled to 29 single layers of NCC in HT model.

Following that, the temperature calculated from each coupled material zones in the HT model is averaged over the entire domain and used as the input for all the EC model in the next calculation time. By this method, Heat and temperature are exchanged for all subsequent times, thereby connecting the two models more accurately than the existing lumped HT models which calculates the overall cell temperature based on the averaging of the thermos-physical properties of the battery

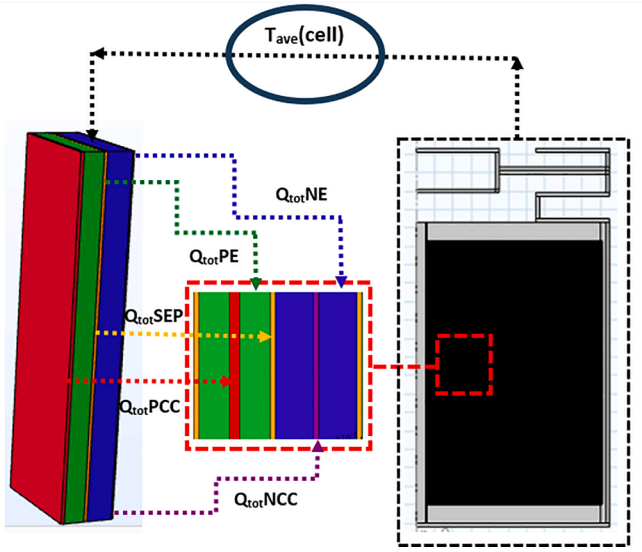

Fig. 2. A coupled 3D EC model and 2D axi-symmetric HT model.

material components.

3. Results and discussion

3.1. Model verification and validation

First, to verify our model, mesh independency tests were conducted, and the results showed the convergence of the tabbed 21,700 Li-ion model with 5,883 domain elements, 5,585 boundary elements, and 1,387 edge elements for a converged cell voltage in Fig. 3 (a). Whereas 28,047 domain elements and 23,559 boundary elements are required for a converged surface temperature in Fig. 3 (b). In addition, for the tabless model, further mesh refinement was carried out to account for the continuous tab configurations. Thus, considering the computational costs, the meshes used in this study are fine enough to verify our model. To further verify the model accuracy and explore a way to reduce the computational times, the time step independence verification studies are conducted as shown in Fig. 3 (c). The time-step sizes are chosen as t3 = 3000 s, t2 = 300 s, and t1 = 30 s, and cell voltage discharge and surface temperatures are calculated at 1C-rate for each timestep. It is obvious that the trend of cell voltages and surface temperature curves overlap at all timesteps, but the magnitude for t1 deviated further away from t2 and t3. Therefore, the two-step t2 = 300 s was chosen to ensure a good balance between model accuracy and computational time cost.

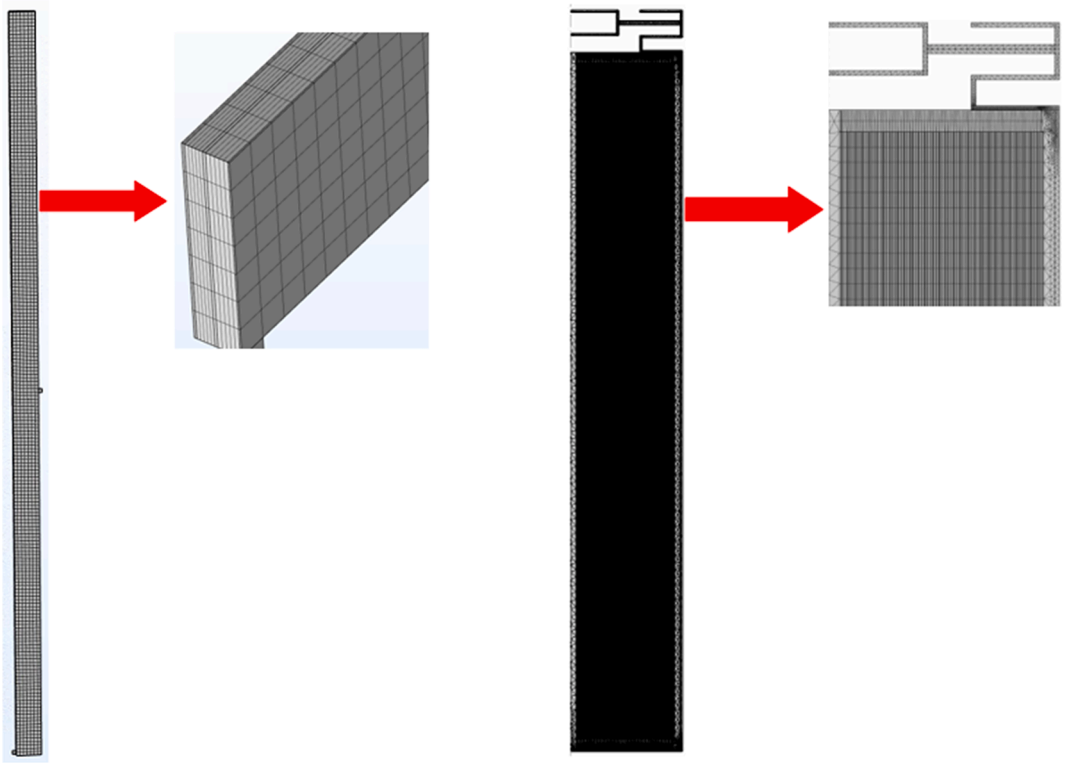

Fig. 3. Mesh tests for a converged (a) cell voltage and (b) surface temperature; (c) timestep test; Model validation for tabbed cells at different discharge rates using P2D model for (d) cell voltage and (e) surface temperature; and using 3D disassembled EC model; (f) cell voltage and (g) surface temperature.

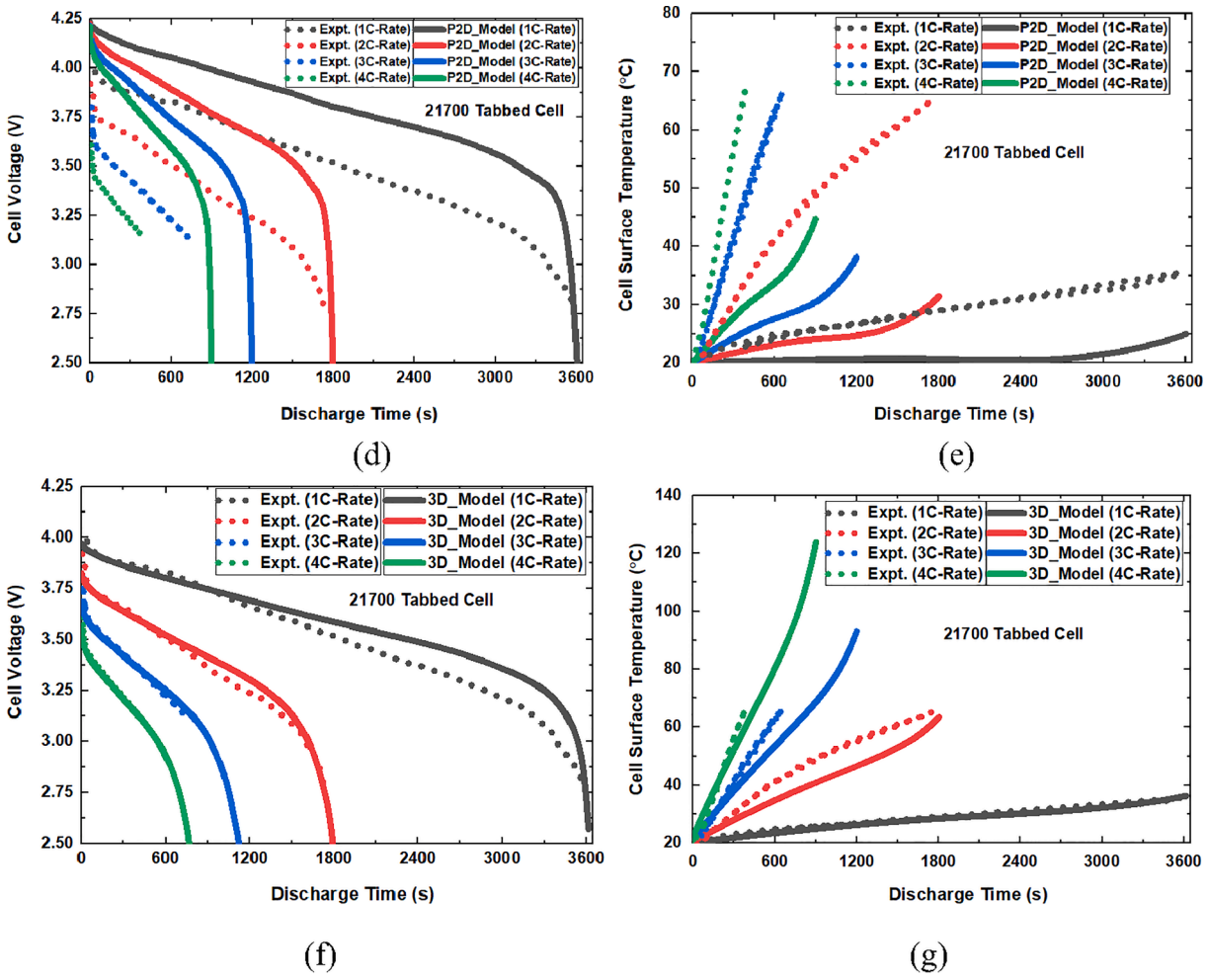

Fig. 3. (*continued*).

To validate our model, the cell voltage and surface temperature variations of a tabbed cell is simulated at various discharge rates and validated by discharge experiments [48,54]. First, we tested the traditional, more simplistic, and faster P2D model, to capture the cell voltage discharge and surface temperature variations of a tabbed cell at various discharge rates and compared the results with experimental data. The P2D model, often known as the Doyle-Fuller-Newman (DFN) model, is a widely recognized physics-based model in the battery modelling community. And although it is widely utilized and effective in battery design, optimization, and performance prediction, this model neglects the non-homogeneities within the electrode plane of the battery component and the effects of current collector completely. These result in significant errors when applied to large cylindrical batteries like the 21,700 cells [54] or when considering cell's shape, location, and quantity of the tabs [56], thus making it nearly impossible to study tabless designs, which is the focus of the present study. Fig. 3(d-e) present comparisons between the experimental and numerical results obtained using P2D model EC coupled with the 2D axisymmetric thermal model at various discharge protocols (1C–4C). The results reveal unacceptable discrepancies between the experimental and simulated results both in the cell voltage discharge and surface temperature profiles which make the model unsuitable for this study. Next, the newly developed 3D disassembled EC model is tested and compared with the same experimental data at same discharge rates (1C–4C) as with P2D model. Fig. 3(f) reveals that the simulated voltage curve for 3D disassembled EC model agrees well with the experimental data, with the maximum voltage deviation of less than 5 %. Also, the simulated surface temperature (i.e., average temperature on the outer surface of the cylindrical battery) at different discharge rates is compared to the measured values in Fig. 3(g), and the results are essentially consistent both in trend and magnitude. On the other hand, it is important to state that the discharge experiments were stopped automatically when the battery temperature reached 65 °C, which is slightly higher than the manufacturer's recommended safe temperature zone for the corresponding commercial cell (60 °C) [54]. And as a result, the experimental curves at 3C and 4C discharge rates are incomplete. Although the analysis does not fit perfectly well with the experimental cell voltage and temperature results in terms of the magnitudes, nevertheless, it captured appropriately their general trends. Furthermore, because our goal is to understand the heat generation behaviors of the 21,700 tabless cells, simulation results at higher discharge rates can provide useful information for the optimal design of the 21,700 tabless cells under fast charging protocols. This will be covered in greater detail in the results section.

4.

4.1. Comparison of the heat generation for tabbed and tabless designs

According to previous research, one of the main factors influencing the high-rate performance of tabbed cells is high ohmic impedance on the current collectors [56]. As a result, lowering the ohm drop on the current collectors is therefore an effective technique. Rather than

increasing the current collector thickness, which may reduce cell specific energy density, optimizing the tab layout is a more efficient way to solve this problem. In this section, the contribution to the total heat generation rate from each material component that makes up the tabbed and tabless batteries during moderate discharge rates under natural (5 $W/(m^2 \cdot K)$) and forced (25 $W/(m^2 \cdot K)$) convections are shown in Fig. 4(a-c). While the cell voltage discharge and the surface temperature are shown in Fig. 4(d) and Fig. 4(e) respectively, and the total heat generation summary is shown in Fig. 4(f). The results unveil that at 1 C-rate and higher, heat generation in the tabbed design is much higher than in

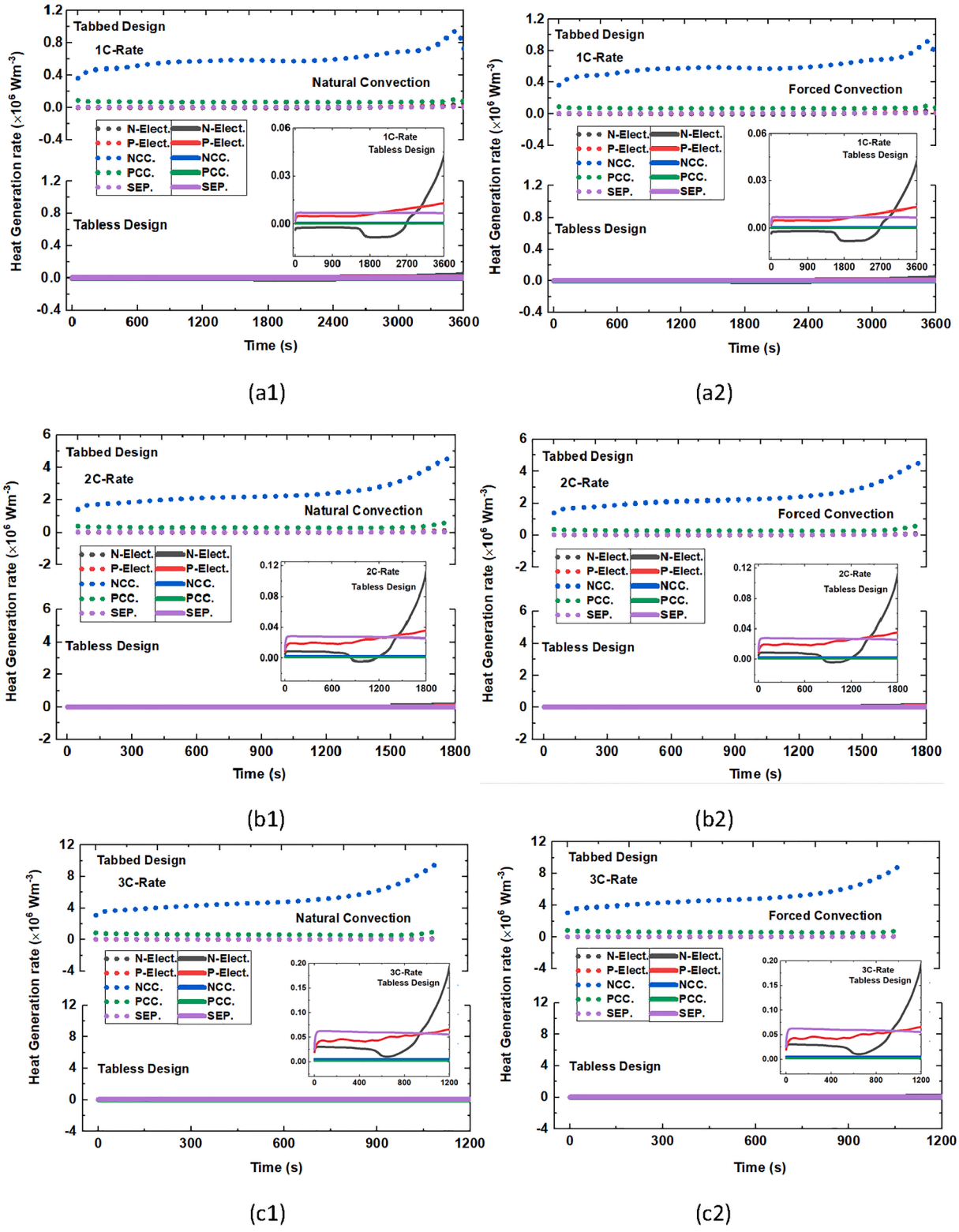

Fig. 4. Comparison of the total heat generation from each material component of the tabbed and tabless cell designs at (1) natural convection and (2) forced convection for; (a) 1C-rate, (b) 2C-rate, (c) 3C-rate; (d) cell voltage @ 1-3C-Rates; (e) Surface temperature @ 1-3C-Rates (f) Total heat generation rate summary, and (g) temperature contour of (g1) tabbed and (g2) tabless cylindrical Li-ion batteries at 3C-rate.

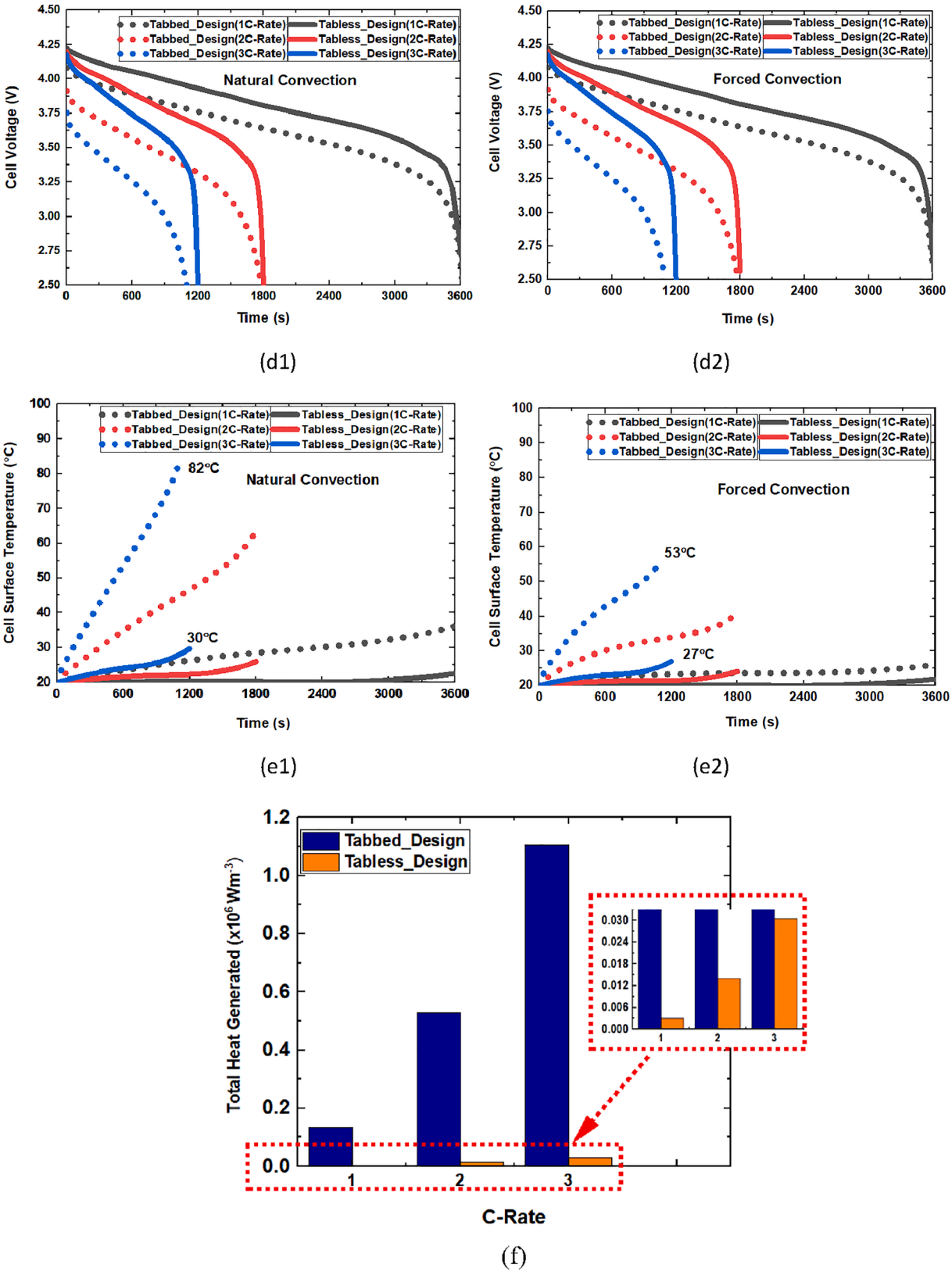

Fig. 4. (*continued*).

the tabless design, with the tabbed NCCs generating the bulk of the heat. In addition, the heat generated at the PCC of the tabbed design is also higher than that of the tabless design, with around half that amount. Furthermore, regardless of the cooling circumstances, both the heat production rate and the cell voltage discharge show similar patterns, indicating that the cooling method has a negligible effect on the heat generation rate and the electrochemical processes of the battery. This phenomenon is also documented by Xie et al. [57]. Conversely, in natural convection, the temperature profiles on the cell surface are considerably higher than those in forced convection due to the more

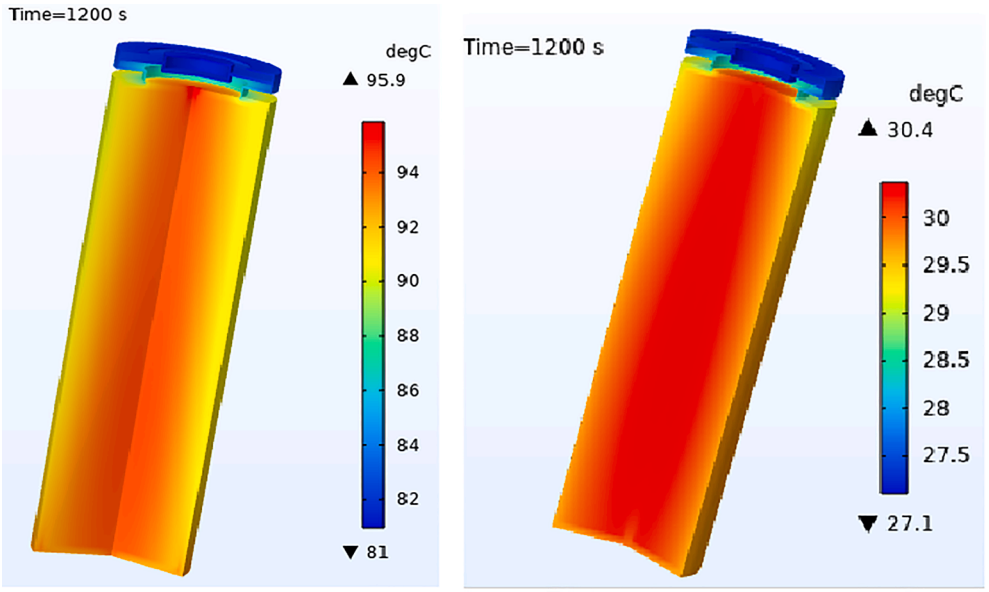

(g1) (g2)

Fig. 4. (*continued*).

rapid dissipation of heat. In addition, the tabbed design is more efficient in dispersing heat under forced convection compared to the tabless design, resulting in a surface temperature decrease of 29 °C at 3C-rate, as opposed to just 3 °C in the tabless design. Fig. 4(g) depicts the temperature distribution of the tabbed and tabless cells at a discharge rate of 3C. It reveals that while heat is generated in the battery's jellyroll, leading to elevated temperatures near the battery's core, the temperature variation within the battery, from its inner core to its outer surface, is notably more significant in tabbed design than the tabless concept. In general, the absence of tabs in a design can significantly decrease the distance that electrons travel on current collectors. This leads to a more even distribution of current density and utilization rate of active materials. Additionally, it reduces the drop in cell voltage caused by ohmic impedance and promotes a more uniform cell temperature. This is an important factor to consider in BTMS [31].

4.2. Thermal properties

4.2.1. Effects of electrode particle radius on heat generation

The effect of the active material particle size on the heat generation rate of total, ohmic, polarization, and reversible heats is systematically studied in this section, under 10 C discharge for various particle radii. In this study, we define $rp_{new} = \omega \times rp_{original}$, where ω is the so-called particle size miniaturisation factor, $rp_{original} and rp_{new}$ are the original and new electrode particle radii respectively.

As shown in Fig. 5, the polarisation heat generation rate is the dominant heat source in the NE while ohmic heating dominates heat source in the PE as ω goes from 1 to 0.25. At the beginning of the discharge process, the polarisation heat increases gradually in the NE, and sharply towards the end of life around DoD = 80 %, whereas in the PE the polarisation heat rises sharply in the beginning of discharge and around DoD = 10 %, it starts to fluctuate gradually and eventually plateaus towards the end of discharge. Due to their high ionic conductivities, the NE generate less total ohmic heat during discharge compared to the PE, given the same discharge current and ω. Also, as seen from the graphs, as ω goes from 1 to 0.25, the ohmic heating at the NE decreases initially with ω because the battery is not drawing significant current. As the battery discharges, the current drawn increases and the Li-ion at the NE start to accumulate due to its larger particle radius, causing an increase in resistance and a gradual increase in ohmic heating. At DoD = 36 %, a high increase in ohmic heating causes a reverse in the trend of ω, while at DoD = 80–90 %, the ohmic heating at both electrodes increased drastically as ω decreases. This is because the battery is nearing the end of its useful life and the accumulation of Li-ion at both electrodes become significant. In comparison, the reversible heat of the NE has a significant impact on total heat generation and because the anode's entropy coefficient is much higher than that of the cathode, the negative reversible heat decreases greatly within its sink regime, as ω goes from 1 to 0.25, whereas the positive reversible heat varies little with ω. In particular, the reversible heat generation in the NE changes from a heat sink to a heat source after the DOD reaches 88 %, with fluctuations which increase with ω, whereas in the PE, the reversible heat (though of a lower magnitude than the NE) remains unchanged with ω and are all within the heat source regimes.

In summary, the total average volumetric polarisation heat generation rate during discharge decreases from $+ 30 \times 10^6\ Wm^{-3}$ to $+ 10 \times 10^6\ Wm^{-3}$ in the NE and $+ 10 \times 10^6\ Wm^{-3}$ to $+ 2 \times 10^6\ Wm^{-3}$ in the PE as ω goes from 1 to 0.25. In contrast, the total average volumetric ohmic heat generation rate shows an increase from $+ 13 \times 10^6\ Wm^{-3}$ to $+ 23 \times 10^6\ Wm^{-3}$ in the NE and $+ 22.5 \times 10^6\ Wm^{-3}$ to $+ 39 \times 10^6\ Wm^{-3}$ in the PE as ω goes from 1 to 0.25. Interestingly, the total average volumetric reversible heat generation rate shows a decrease from $-5 \times 10^6\ Wm^{-3}$ to $-8 \times 10^6\ Wm^{-3}$ in the NE and remains unchanged in the PE as ω goes from 1 to 0.25. We therefore conclude that the drop in temperature originates mainly from the reversible heat in the anode side and the polarization heat in both electrodes as ω goes from 1 to 0.25, where as the voltage curve is lowered due to the increase in charge transfer polarization.

4.2.2. Effects of electrode thickness on heat generation

Similar to the particle radius, the TH properties are closely related to the material thickness. As a result, the effect of the electrode thickness on the heat generation rate of total, ohmic, polarization, and reversible heats is systematically studied in this section, under 10 C discharge for various particle radii. In this study, we define $t_{new} = \eta \times t_{original}$, where η is the so-called electrode thickness miniaturisation factor, $t_{original} and t_{new}$ are the original and new electrode thicknesses respectively.

As shown in Fig. 6, the electrode thickness miniaturisation factor, η has

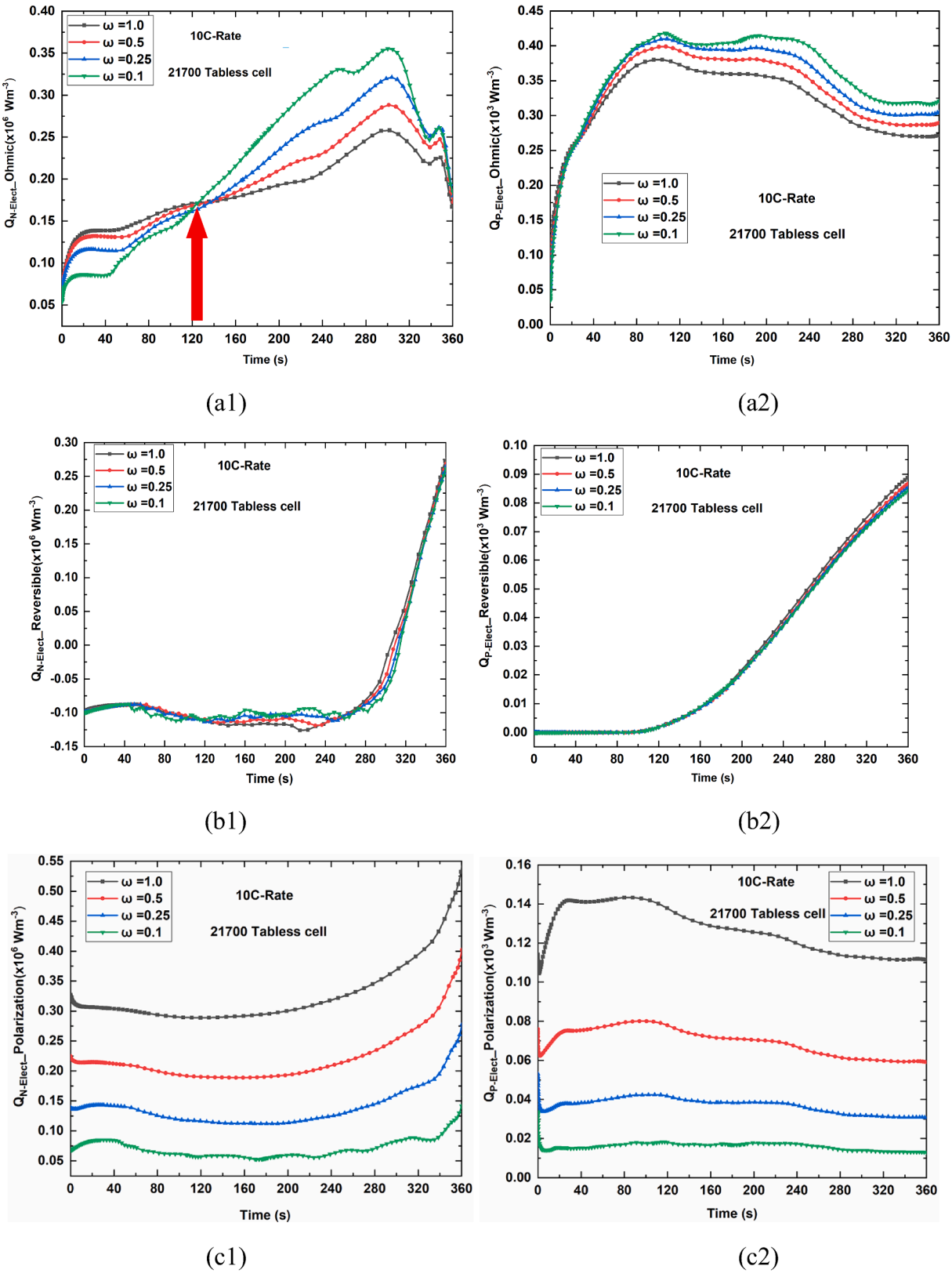

Fig. 5. Average volumetric heat generation rate with different particle sizes in (1) PE and (2) NE; (a) ohmic heat generation; (b) reversible heat generation (c) polarisation heat generation; and (d) summary; (e1) cell voltage and (e2) cell temperature.

the greatest influence on the ohmic heating in both electrodes than the other heat sources. The reason is because a thinner electrode causes electron to traverse a shorter distance leading to a smaller electron resistance [58,59]. The negative reversible heat increases greatly from its sink regime towards source, as η goes from 1 to 0.25, whereas the positive reversible heat varies little with η. In particular, the reversible

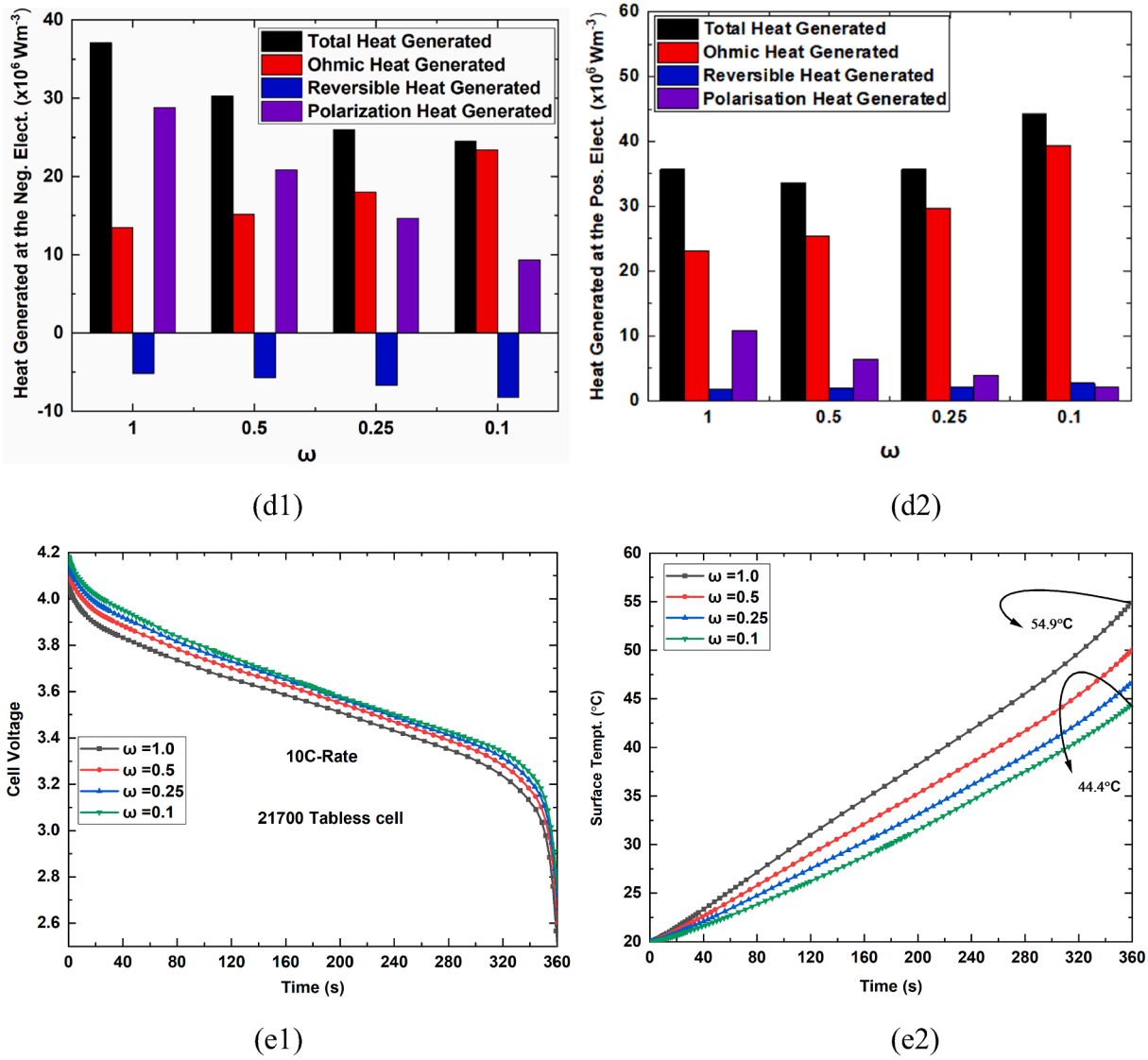

Fig. 5. (*continued*).

heat generation in the NE changes from a heat sink to a heat source after the DOD reaches 80 %, with fluctuations which increase with η, whereas in the PE, the reversible heat remains constant with η and are all within the heat source regimes.

In summary, the total average volumetric polarisation heat generation rate during discharge decreases from $+30 \times 10^6\ Wm^{-3}$ to $+22 \times 10^6\ Wm^{-3}$ in the NE and $+10 \times 10^6\ Wm^{-3}$ to $+5 \times 10^6\ Wm^{-3}$ in the PE as η goes from 1 to 0.25. Also, the total average volumetric ohmic heat generation rate shows a decreased from $+13 \times 10^6\ Wm^{-3}$ to $+0.5 \times 10^6\ Wm^{-3}$ in the NE and $+22.5 \times 10^6\ Wm^{-3}$ to $+1 \times 10^6\ Wm^{-3}$ in the PE as η goes from 1 to 0.25. In contrast to the case of the particle radius effects, the total average volumetric reversible heat generation rate shows a slight increase from $-5 \times 10^6\ Wm^{-3}$ to $-1 \times 10^6\ Wm^{-3}$ in the NE and remains unchanged in the PE as η goes from 1 to 0.25. We therefore conclude that the large drop in temperature (over 35 %) originates mainly from the ohmic and polarisation heat sources in both electrodes, whereas the voltage curve is elevated due to the relatively lower ohmic resistance as η goes from 1 to 0.25.

5. Conclusion

In summary, a 3D EC - HT coupled model is developed for cylindrical type Li-ion batteries to investigate the heat generation mechanisms of various components that make up the battery core. The heat generation behaviours of tabbed and tabless batteries as well as proportion of ohmic, polarization and reversible heats at high discharge rates are analysed quantitatively for each battery component. The effects of particle size and electrode thickness for the tabless design on the various heat sources for the battery's electrodes are investigated at a high discharge rate of 10 C. Based on the above studies, the following conclusions are drawn:

(i). At 1 C-rate and higher, heat generation in the tabbed design is significantly higher than in the tabless design, with the tabbed design's NCCs accounting for over 80 % of the total heats. This follows that a tabless concept drastically reduces the transmission distance of electrons on current collectors, resulting in uniform current density and utilization rate of active materials.

(ii). Polarisation heat decreases significantly in both electrodes as the particle size is miniaturized. The reversible heat in the anode side is negative initially and fluctuates towards the end of life (depth of discharge DOD = 88 %) when it changes from heat sink to heat source, whereas in the cathode it remains unchanged throughout the discharge process.

(iii). The resulting temperature drop is caused by the increase in the overall reversible heat sink effect in the anode side, as well as the

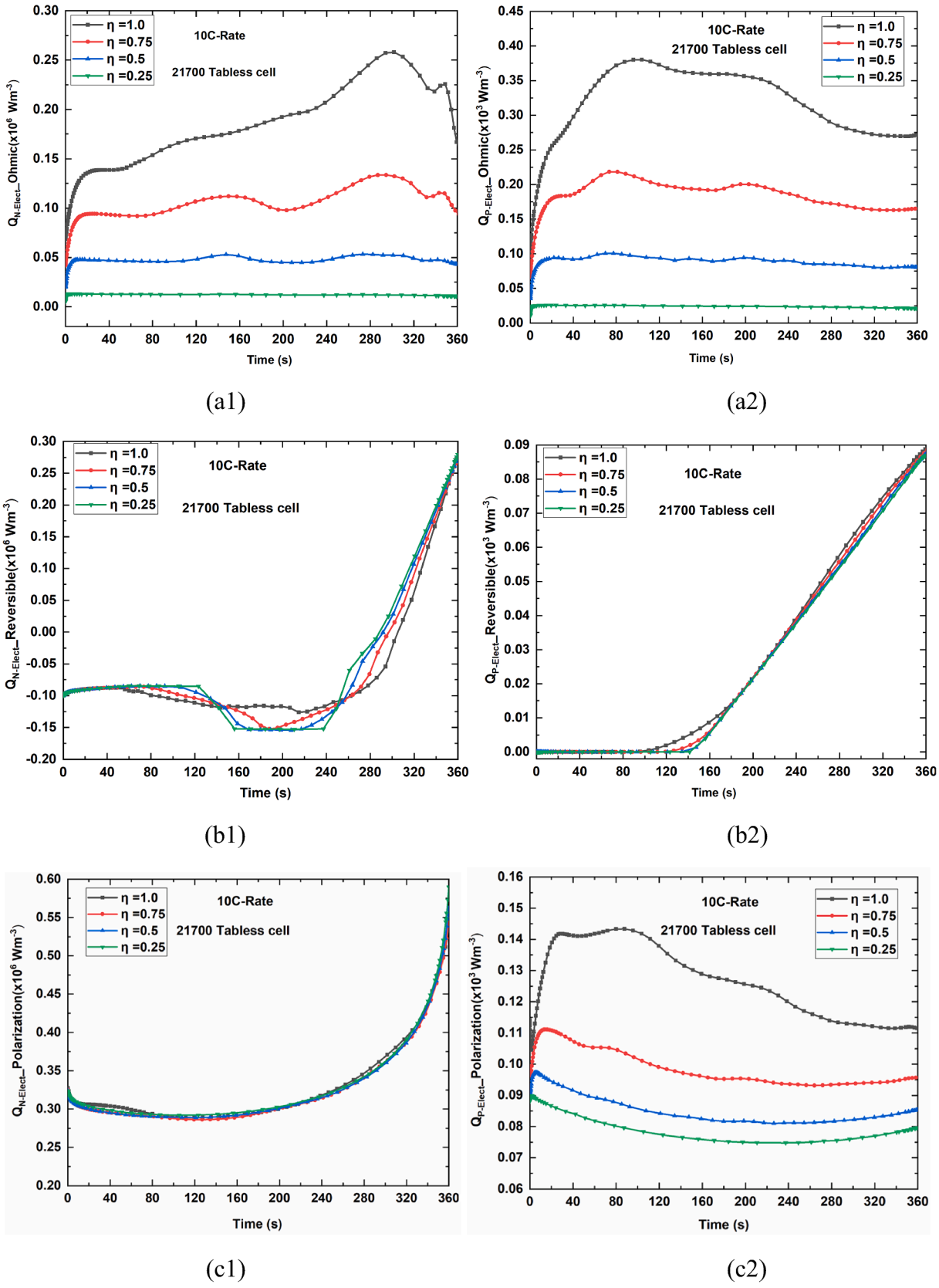

Fig. 6. Average volumetric heat generation rate with different electrode sizes in (1) PE and (2) NE; (a) ohmic heat generation; (b) reversible heat generation (c) polarisation heat generation; and (d) summary; (e1) cell voltage and (e2) cell temperature.

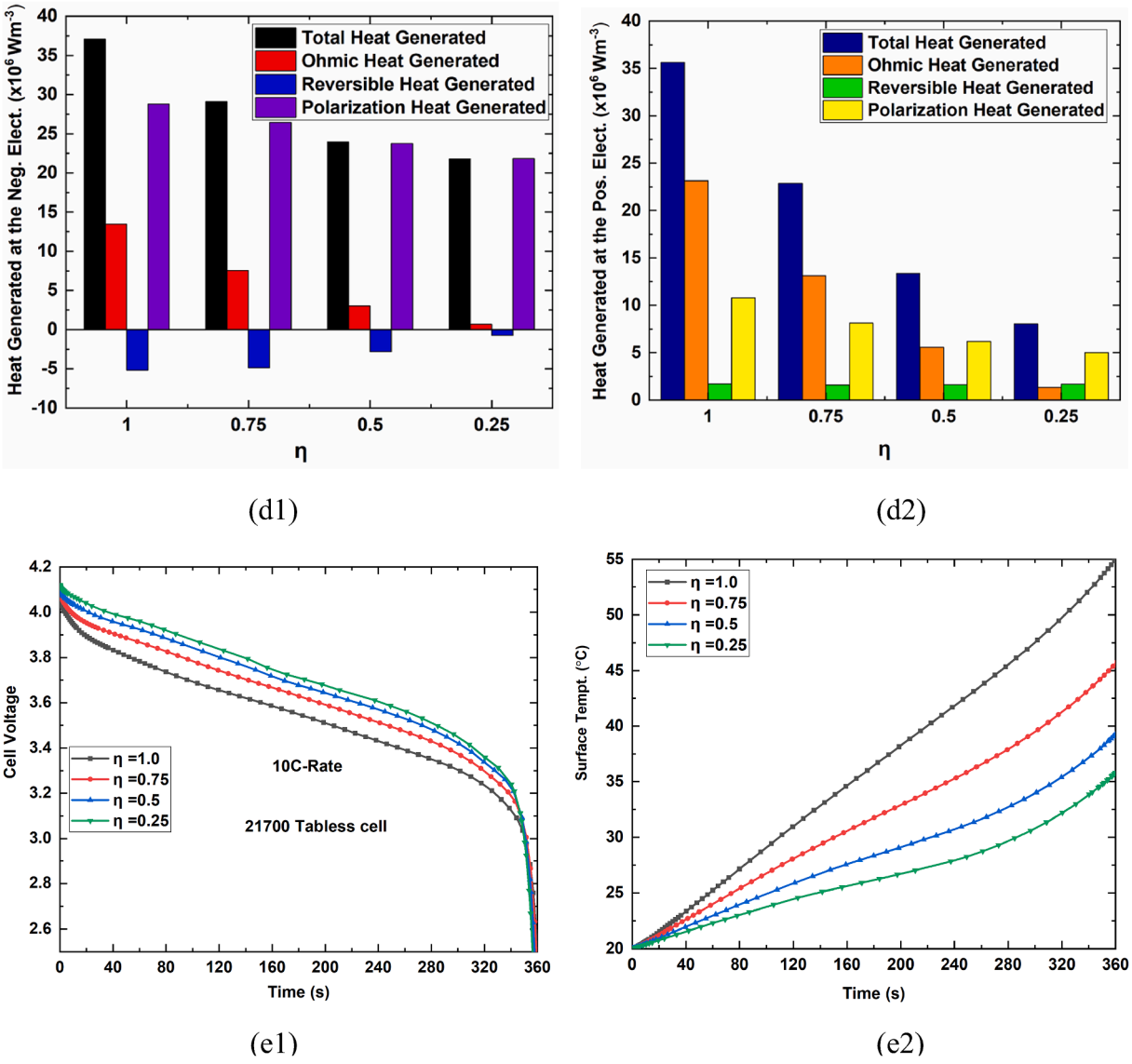

Fig. 6. (*continued*).

weakened polarization heat in both electrodes.

(iv). Miniaturising the electrode thickness causes a considerable decrease in ohmic heating in both electrodes resulting in larger temperature drops.

This work offers more insights into heat generation mechanisms in Li-ion batteries, especially the reversible heat, which has a potential to be tuned to achieve internal cooling of the battery cell to eliminate the need for an expensive and complex battery BTMS.

CRediT authorship contribution statement

Chika Eze: Conceptualization, Formal analysis, Software, Writing – original draft. **Jingyuan Zhao:** Visualization, Writing – review & editing. **Dukhyun Chung:** Data curation, Investigation, Writing – review & editing. **Mohammad Fakhimi Bonab:** Formal analysis, Writing – review & editing. **Abel Chuang:** Supervision, Writing – review & editing. **Andrew F. Burke:** Investigation, Visualization, Writing – review & editing. **Guanhua Chen:** Funding acquisition, Investigation, Supervision.

Declaration of competing interest

The authors declare that they have no known competing financial interests or personal relationships that could have appeared to influence the work reported in this paper.

Data availability

Data will be made available on request.

Acknowledgements

The authors acknowledge the support from the Hong Kong Quantum AI Lab Limited (HKQAI), AIR@InnoHK of Hong Kong government.

References

[1] F. Kong, X. Liu, Sustainable transportation with electric vehicles, Foundations and Trends® in Electric Energy Systems 2 (1) (2017) 1–132.
[2] N.O. Kapustin, D.A. Grushevenko, Long-term electric vehicles outlook and their potential impact on electric grid, Energy Pol. 137 (2020) 111103.
[3] IEA, Global EV Outlook 2022, IEA, Paris, 2022 https://www.iea.org/reports/global-ev-outlook-2022.

[4] M.A. Hannan, M.M. Hoque, A. Mohamed, A. Ayob, Review of energy storage systems for electric vehicle applications: Issues and challenges, Renew. Sustain. Energy Rev. 69 (2017) 771–789.

[5] J. Lin, X. Liu, S. Li, C. Zhang, S. Yang, A review on recent progress, challenges and perspective of battery thermal management system, Int. J. Heat Mass Transf. 167 (2021) 120834.

[6] D. Ouyang, J. Weng, M. Chen, J. Wang, Z. Wang, Electrochemical and thermal characteristics of aging lithium-ion cells after long-term cycling at abusive-temperature environments, Process Saf. Environ. Prot. 159 (2022) 1215–1223.

[7] Q.L. Yue, C.X. He, M.C. Wu, T.S. Zhao, Advances in thermal management systems for next-generation power batteries, Int. J. Heat Mass Transf. 181 (2021) 121853.

[8] Y. Ye, L.H. Saw, Y. Shi, A.AO. Tay, Numerical analyses on optimizing a heat pipe thermal management system for lithium-ion batteries during fast charging, Appl. Therm. Eng. 86 (2015) 281–291.

[9] Zhao, Chunrong, Antonio CM Sousa, Fangming Jiang, Minimization of thermal non-uniformity in lithium-ion battery pack cooled by channeled liquid flow, Int. J. Heat Mass Transfer 129 (2019) 660–670.

[10] Z. Rao, S. Wang, G. Zhang, Simulation and experiment of thermal energy management with phase change material for ageing LiFePO4 power battery, Energ. Conver. Manage. 52 (12) (2011) 3408–3414.

[11] W. Mei, H. Li, C. Zhao, J. Sun, Q. Wang, Numerical study on thermal characteristics comparison between charge and discharge process for lithium-ion battery, Int. J. Heat Mass Transf. 162 (2020) 120319.

[12] T.M. Bandhauer, S. Garimella, T.F. Fuller, A critical review of thermal issues in lithium-ion batteries, J. Electrochem. Soc. 158 (3) (2011) R1.

[13] Z. Rao, Y. Huo, X. Liu, G. Zhang, Experimental investigation of battery thermal management system for electric vehicle based on paraffin/copper foam, J. Energy Inst. 88 (3) (2015) 241–246.

[14] G.M. Cavalheiro, T. Iriyama, G.J. Nelson, S. Huang, G. Zhang, Effects of nonuniform temperature distribution on degradation of lithium-ion batteries, J. Electrochem. Energy Convers. Storage 17, no. 2 (2020).

[15] M. Xu, R. Wang, B. Reichman, X. Wang, Modeling the effect of two-stage fast charging protocol on thermal behavior and charging energy efficiency of lithium-ion batteries, J. Storage Mater. 20 (2018) 298–309.

[16] M. Khamar, J. Askari, A charging method for Lithium-ion battery using Min-max optimal control, in: In 2014 22nd Iranian Conference on Electrical Engineering (ICEE), 2014, pp. 1239–1243.

[17] Guo, Zhen, Bor Yann Liaw, Xinping Qiu, Lanlan Gao, and Changshui Zhang, Optimal charging method for lithium ion batteries using a universal voltage protocol accommodating aging, J. Power Sources 274 (2015) 957–964.

[18] M. Hussain, M.K. Khan, M. Pathak, Thermal analysis of phase change material encapsulated li-ion battery pack using multi-scale multi-dimensional framework, J. Storage Mater. 65 (2023) 107290.

[19] C. Zou, C. Manzie, D. Nešić, PDE battery model simplification for charging strategy evaluation, in: In 2015 10th Asian Control Conference (ASCC), 2015, pp. 1–6.

[20] S. Pramanik, S. Anwar, Electrochemical model based charge optimization for lithium-ion batteries, J. Power Sources 313 (2016) 164–177.

[21] S.K. Rahimian, S.C. Rayman, R.E. White, Maximizing the life of a lithium-ion cell by optimization of charging rates, J. Electrochem. Soc. 157 (12) (2010) A1302.

[22] M. Xu, Z. Zhang, X. Wang, L.i. Jia, L. Yang, A pseudo three-dimensional electrochemical–thermal model of a prismatic LiFePO4 battery during discharge process, Energy 80 (2015) 303–317.

[23] S. Panchal, I. Dincer, M. Agelin-Chaab, R. Fraser, M. Fowler, Experimental and theoretical investigations of heat generation rates for a water cooled LiFePO4 battery, Int. J. Heat Mass Transf. 101 (2016) 1093–1102.

[24] Z. Rao, S. Wang, A review of power battery thermal energy management, Renew. Sustain. Energy Rev. 15 (9) (2011) 4554–4571.

[25] I.A. Hunt, Y. Zhao, Y. Patel, G.J. Offer, Surface cooling causes accelerated degradation compared to tab cooling for lithium-ion pouch cells, J. Electrochem. Soc. 163 (9) (2016) A1846.

[26] T. Waldmann, G. Geramifard, M. Wohlfahrt-Mehrens, Influence of current collecting tab design on thermal and electrochemical performance of cylindrical Lithium-ion cells during high current discharge, J. Storage Mater. 5 (2016) 163–168.

[27] H. Park, A design of air flow configuration for cooling lithium ion battery in hybrid electric vehicles, J. Power Sources 239 (2013) 30–36.

[28] S. Panchal, K. Gudlanarva, M.-K. Tran, R. Fraser, M. Fowler, High reynold's number turbulent model for micro-channel cold plate using reverse engineering approach for water-cooled battery in electric vehicles, Energies 13 (7) (2020) 1638.

[29] M.S. Patil, J.-H. Seo, S. Panchal, M.-Y. Lee, Numerical study on sensitivity analysis of factors influencing liquid cooling with double cold-plate for lithium-ion pouch cell, Int. J. Energy Res. 45 (2) (2021) 2533–2559.

[30] N. Yang, X. Zhang, G. Li, D. Hua, Assessment of the forced air-cooling performance for cylindrical lithium-ion battery packs: a comparative analysis between aligned and staggered cell arrangements, Appl. Therm. Eng. 80 (2015) 55–65.

[31] Khan, Shahid Ali, Chika Eze, Kejian Dong, Ali Raza Shahid, Mahesh Suresh Patil, Shakeel Ahmad, Iftikhar Hussain, and Jiyun Zhao. "Design of a new optimized U-shaped lightweight liquid-cooled battery thermal management system for electric vehicles: A machine learning approach." International Communications in Heat and Mass Transfer 136 (2022): 106209.

[32] H. Liu, E. Chika, J. Zhao, Investigation into the effectiveness of nanofluids on the mini-channel thermal management for high power lithium ion battery, Appl. Therm. Eng. 142 (2018) 511–523.

[33] Y. Zhao, Y. Patel, T. Zhang, G.J. Offer, Modeling the effects of thermal gradients induced by tab and surface cooling on lithium ion cell performance, J. Electrochem. Soc. 165 (13) (2018) A3169.

[34] R.E. Ciez, J.F. Whitacre, Comparison between cylindrical and prismatic lithium-ion cell costs using a process based cost model, J. Power Sources 340 (2017) 273–281.

[35] T. Hettesheimer, A. Thielmann, C. Neef, K.-C. Möller, and M. Wolter, https://www.batterien.fraunhofer.de/content/dam/batterien/de/documents/Allianz_Batterie_Zellformate_Studie.pdf. (2017). Accessed 11th Oct 2022.

[36] J. Sturm, A. Frank, A. Rheinfeld, S.V. Erhard, A. Jossen, Impact of electrode and cell design on fast charging capabilities of cylindrical lithium-ion batteries, J. Electrochem. Soc. 167 (13) (2020) 130505.

[37] A. Rheinfeld, J. Sturm, A. Frank, S. Kosch, S.V. Erhard, A. Jossen, Impact of cell size and format on external short circuit behavior of lithium-ion cells at varying cooling conditions: modeling and simulation, J. Electrochem. Soc. 167 (1) (2019) 013511.

[38] A. Frank, J. Sturm, M. Steinhardt, A. Rheinfeld, A. Jossen, Impact of current collector design and cooling topology on fast charging of cylindrical lithium-ion batteries, ECS Advances 1 (4) (2022) 040502.

[39] Li, Shen, Niall Kirkaldy, Cheng Zhang, Krishnakumar Gopalakrishnan, Tazdin Amietszajew, Laura Bravo Diaz, Jorge Varela Barreras et al., Optimal cell tab design and cooling strategy for cylindrical lithium-ion batteries, J. Power Sources 492 (2021) 229594.

[40] K.-J. Lee, K. Smith, A. Pesaran, G.-H. Kim, Three dimensional thermal-, electrical-, and electrochemical-coupled model for cylindrical wound large format lithium-ion batteries, J. Power Sources 241 (2013) 20–32.

[41] K. Tsuruta, M.E. Dermer, R. Dhiman. Cell with a tabless electrode, 16/673464 https://patents.google.com/patent/US20200144676A1/en/ (2020), Accessed 10th Oct 2022.

[42] A. Jokar, B. Rajabloo, M. Désilets, M. Lacroix, Review of simplified Pseudo-two-Dimensional models of lithium-ion batteries, J. Power Sources 327 (2016) 44–55.

[43] M. Doyle, J. Newman, The use of mathematical modeling in the design of lithium/polymer battery systems, Electrochim. Acta 40 (13–14) (1995) 2191–2196.

[44] M. Doyle, T.F. Fuller, J. Newman, Modeling of galvanostatic charge and discharge of the lithium/polymer/insertion cell, J. Electrochem. Soc. 140 (6) (1993) 1526.

[45] M. Doyle, J. Newman, A.S. Gozdz, C.N. Schmutz, J.-M. Tarascon, Comparison of modeling predictions with experimental data from plastic lithium ion cells, J. Electrochem. Soc. 143 (6) (1996) 1890.

[46] V. Ramadesigan, P.WC. Northrop, S. De, S. Santhanagopalan, R.D. Braatz, V. R. Subramanian, Modeling and simulation of lithium-ion batteries from a systems engineering perspective, J. Electrochem. Soc. 159 (3) (2012) R31.

[47] C.X. He, Q.L. Yue, M.C. Wu, Q. Chen, T.S. Zhao, A 3D electrochemical-thermal coupled model for electrochemical and thermal analysis of pouch-type lithium-ion batteries, Int. J. Heat Mass Transf. 181 (2021) 121855.

[48] J.B. Quinn, T. Waldmann, K. Richter, M. Kasper, M. Wohlfahrt-Mehrens, Energy density of cylindrical Li-ion cells: a comparison of commercial 18650 to the 21700 cells, J. Electrochem. Soc. 165 (14) (2018) A3284.

[49] J. Newman, W. Tiedemann, Porous-electrode theory with battery applications, AIChE J 21 (1) (1975) 25–41.

[50] T.-S. Dao, C.P. Vyasarayani, J. McPhee, Simplification and order reduction of lithium-ion battery model based on porous-electrode theory, J. Power Sources 198 (2012) 329–337.

[51] S. Panchal, M. Mathew, R. Fraser, M. Fowler, Electrochemical thermal modeling and experimental measurements of 18650 cylindrical lithium-ion battery during discharge cycle for an EV, Appl. Therm. Eng. 135 (2018) 123–132.

[52] Y. Ye, Y. Shi, N. Cai, J. Lee, X. He, Electro-thermal modeling and experimental validation for lithium ion battery, J. Power Sources 199 (2012) 227–238.

[53] K. Somasundaram, E. Birgersson, A.S. Mujumdar, Thermal–electrochemical model for passive thermal management of a spiral-wound lithium-ion battery, J. Power Sources 203 (2012) 84–96.

[54] L. Yin, A. Björneklett, E. Söderlund, D. Brandell, Analyzing and mitigating battery ageing by self-heating through a coupled thermal-electrochemical model of cylindrical Li-ion cells, J. Storage Mater. 39 (2021) 102648.

[55] Sharma, Ashwini Kumar, Karthik Somasundaram, Erik Birgersson, Wei Tong, Huan Viet Nguyen, Adrian Fisher, and Arun Sadashiv Mujumdar. "Scale analysis of electrochemical and thermal behaviour of a cylindrical spiral-wound lithium-ion battery." Electrochimica Acta 400 (2021): 139397.

[56] F.-Q. An, W.-N. Zhou, P. Li, Modeling and validation on the respective contributions of positive and negative tabs for 18650 cell, J. Storage Mater. 20 (2018) 439–450.

[57] Y. Xie, S. Shi, J. Tang, W.u. Hongwei, Y.u. Jianzu, Experimental and analytical study on heat generation characteristics of a lithium-ion power battery, Int. J. Heat Mass Transf. 122 (2018) 884–894.

[58] W. Lu, A. Jansen, D. Dees, P. Nelson, N.R. Veselka, G. Henriksen, High-energy electrode investigation for plug-in hybrid electric vehicles, J. Power Sources 196 (3) (2011) 1537–1540.

[59] S.-H. Yu, C.-K. Park, H.o. Jang, C.-B. Shin, W.-I. Cho, Prediction of lithium diffusion coefficient and rate performance by using the discharge curves of LiFePO 4 materials, Bull. Kor. Chem. Soc. 32 (3) (2011) 852–856.